A finite volume method for two-dimensional transonic potential flow through turbomachinery blade rows

J. V. Soulis*

To predict inviscid transonic flow through turbomachinery blade rows, the exact transonic potential flow equation is solved on a mesh constructed from small area elements. A transformation is introduced through which distorted squares of the physical plane are mapped into computational squares. Two sets of overlapping elements are used; while the thermodynamic properties are calculated at the primary element centres, the flux balance is established on the secondary elements. For transonic flows an artificial compressibility term (upwind density gradient) is added to density in order to produce the desired directional bias in the hyperbolic region, while the entropy does not increase across mass conservative shock jump regions. Comparisons with experiments and with other numerical and analytical solutions for various turbomachinery configurations show that this approach is comparatively accurate, reliable, and fast.

Keywords: turbines, compressible flow, finite volume methods

In recent years significant advances have been made in computational fluid dynamics applied to turbomachinery. Many approaches have been taken to the general problem of turbomachinery flow. The purpose of this investigation is to develop an efficient numerical algorithm for the calculation of 2-D potential incompressible and compressible, transonic inviscid flows through turbomachinery blade rows.

A major difficulty in solving the exact potential flow equation lies in the construction of sufficiently accurate discrete approximations to the boundary conditions. A mesh may be constructed from small cells (volumes) which are packed around the turbomachinery blades and cover the whole blade to blade area (sl) surface, shown in Fig 1. Then a transformation is introduced through which the cells of the physical plane are mapped into computational squares. The numerical scheme is constructed using two sets of overlapping cells. The thermodynamic properties are calculated at the centres of the primary cells and then the flux balance is established on the secondary cells. For supersonic regions of the flow-field, a modified density is used instead of the physical density as suggested by Hafez *et al*[1].

The scheme used can be regarded as a combination of the numerical techniques of finite-elements and finite-differences; 'finite-volume' seems an appropriate name. The main features of the numerical scheme are that it preserves the practicability of the finite-element method of setting an irregular computational grid to fit a particular flow-field problem and to modify it with ease, if necessary, and it makes use of the simple analysis of finite-difference methods.

Computations of 2-D, blade to blade inviscid, transonic flow can be formulated, inter alia, in terms of either the Euler equation or the fully potential equations. To solve Euler's equations Gopalakrishnan[2] applied the numerical scheme proposed by MacCormack comprising two steps (predictor and corrector) while Denton[3] used a time marching method based on a finite-volume technique.

Full potential, transonic equation solutions were reported by Caspar *et al*[4] where a general non-orthogonal mesh was used; Acay and Ecer[5] used the

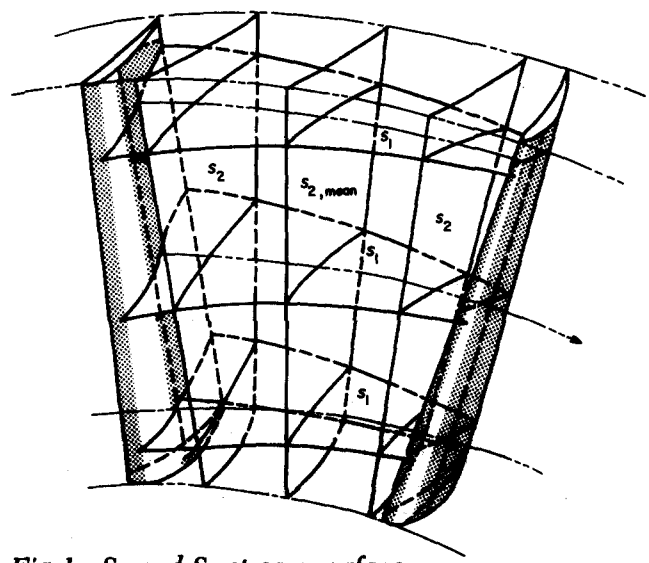

Fig 1 S_1 *and* S_2 *stream surfaces*

* Whittle Laboratory, Department of Engineering, University of Cambridge, Cambridge, England. Presently at Fluid Mechanics/Hydraulics Division, Civil Engineering Department, Demokrition University of Thrace, Xanthi, Greece
Received on 27 August 1982 and accepted for publication on 5 September 1983

 0142-727X/83/040229-09$03.00

finite element method; Habashi *et al*[6] used a finite-element approach with a scheme based upon approximate mapping of a blade into a near circle; Farrell and Adamczyck[7] also used conformal transformation to generate the grid around the cascade blades.

Flow equations

The flow will be assumed to be two-dimensional, inviscid, potential and steady, but with no restriction to subsonic flow. Thus the governing flow equations for the physical domain, where the Cartesian coordinate system is introduced, are,

$$\frac{\partial(\tilde{\rho}u)}{\partial x}+\frac{\partial(\tilde{\rho}v)}{\partial y}=0 \tag{1}$$

$$u=\frac{\partial\Phi}{\partial x} \qquad v=\frac{\partial\Phi}{\partial y} \tag{2}$$

$$q=(u^2+v^2)^{1/2} \tag{3}$$

$$T_{o1}=\text{constant} \tag{4}$$

$$p_{o1}=\text{constant} \tag{5}$$

$$p=p_{o1}\left(\frac{\rho}{\rho_{o1}}\right)^{\gamma} \tag{6}$$

$$\rho=\rho_{o1}\left(1-\frac{q^2}{2c_pT_{o1}}\right)^{1/\gamma-1} \tag{7}$$

and, as will be proved later:

$$\left.\begin{aligned}&\tilde{\rho}=\rho-\mu\frac{\partial\rho}{\partial s}\Delta s\\&\frac{\partial\rho}{\partial s}\Delta s=\frac{u}{q}\delta\rho_x\,\Delta x+\frac{v}{q}\delta\rho_y\,\Delta y\end{aligned}\right\} \tag{8}$$

with

$$\mu=\max\left[0,\left(1-\frac{1}{M^2}\right)\mathrm{k}\right]$$

No assumption will be made about the geometry of the blade row. The problem must be closed with a complete specification of the boundary conditions.

Complex turbomachinery geometries present difficulty when attempting to prescribe the geometry on an orthogonal computational mesh, such as the Cartesian form. Difficulties can arise because the grid points do not adequately describe the blade boundaries. A body fitted non-orthogonal local coordinate system was used to avoid the problems associated with a conventional grid system. Thus the flow field is divided into multiple blocks to accommodate all boundary surface discontinuities and to provide good boundary fitting. This finite-element approach is well adapted to turbomachinery flows for a number of reasons. A wide range of finite elements is possible for adequate description of the surface boundaries and minimal additional computational code logic is required for changing a particular element to a more sophisticated one. There is an automatic treatment of the various forms of the applied boundary conditions.

Notation

a	Local speed of sound (m/s)
a_{ij}	Transformation weighting coefficients
c_p	Coefficient of specific heat at constant pressure (kJ/kg K)
c_v	Coefficient of specific heat at constant volume (kJ/kg K)
c_x	Axial blade chord (m)
G	Matrix of geometrical coefficients
g_{ij}	Elements of the G matrix
g^{ij}	Elements of the G^{-1} matrix
H	Transformation matrix from Cartesian to local ξ, η system
h	Determinant of the H matrix
i, j	Logical indices of mesh variables along η, ξ directions
k	Constant (Eq (8))
M	Local Mach number
N_i	Shape functions
p	Pressure (N/m^2)
p	Pitch (m)
Q	Total velocity in computational plane (m/s)
q	Total velocity (m/s)
R	Gas constant (kJ/kg K)
s	Streamwise direction (m)
T	Temperature (K)
U, V	Contravariant velocity components along the ξ, η directions (m/s)
u, v	Cartesian velocity components along the x, y directions (m/s)
x, y	Cartesian coordinate position along the axial and pitchwise directions (m)
β_1	Inlet flow angle measured from the axial direction (degrees)
γ	Specific heat ratio
μ	Artificial compressibility
ξ, η	Transformed coordinate directions (m)
ρ	Density (kg/m^3)
$\left.\begin{matrix}hU\rho\\hV\rho\end{matrix}\right\}$	Mass fluxes along the ξ, η directions (kg/s)
Φ	Potential (m^2/s)

Subscripts

is	Isentropic
o	Stagnation value
1, 2	Upstream, downstream

Superscripts

T	Transpose matrix
−1	Inverse matrix
*	Sonic condition
~	Modified value

For an iterative approach these boundary conditions can be applied explicitly, ie from the previous iteration, and/or implicitly ie initially set forth. Moreover a single analysis can generate several finite-difference techniques which are dependent on the finite-element selection.

General transformation

The essence of this numerical scheme is that distorted squares in the physical domain will be separately mapped to squares in the computational domain by independent transformations from Cartesian x, y to local ξ, η coordinates (Fig 2). The distorted squares are packed around the blades (Fig 6) and cover the blade to blade area. A primary cell, which is a distorted square in the physical plane or just a square in the computational plane, is formed by eight nodes (Fig 3) while a secondary cell interlocks with nine primary cells. Thus the nodes of the secondary cell are the centres of the surrounding primary cells. Shifts of plus or minus one yield the centroid position of the next secondary cell.

If x_i, y_i are the Cartesian coordinates of a cell, then any coordinates of the cell can be expressed as:

$$x = \sum_{i=1}^{8} N_i x_i \qquad y = \sum_{i=1}^{8} N_i y_i \tag{9}$$

where N_i are the shape functions associated with the cell nodes. The shape functions are defined in terms of a local non-orthogonal coordinate system ξ, η as:

$$\begin{aligned}
N_1 &= \frac{(1-\xi)(1-\eta)(-\xi-\eta-1)}{4} \\
N_2 &= \frac{(1+\xi)(1-\eta)(\xi-\eta-1)}{4} \\
N_3 &= \frac{(1+\xi)(1+\eta)(\xi+\eta-1)}{4} \\
N_4 &= \frac{(1-\xi)(1+\eta)(-\xi+\eta-1)}{4} \\
N_5 &= \frac{(1-\xi^2)(1-\eta)}{2} \\
N_6 &= \frac{(1-\eta^2)(1+\xi)}{2} \\
N_7 &= \frac{(1-\xi^2)(1+\eta)}{2} \\
N_8 &= \frac{(1-\eta^2)(1-\xi)}{2}
\end{aligned} \tag{10}$$

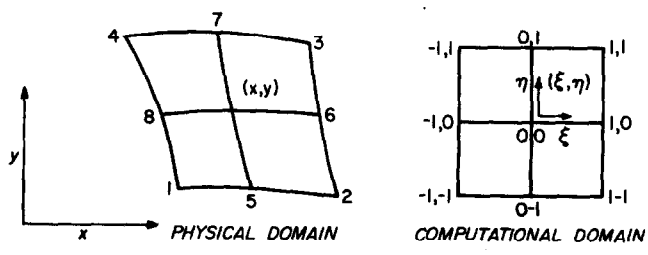

Fig 2 Distorted squares mapped into squares

The local coordinates lie in the range $-1 \leq \xi \leq 1, -1 \leq \eta \leq 1$ so that the vertices of the square are at $\xi = \pm 1 \eta = \pm 1$.

Let H be the transformation matrix from the physical system to the computational local coordinate system:

$$H = \begin{vmatrix} \frac{\partial x}{\partial \xi} & \frac{\partial x}{\partial \eta} \\ \frac{\partial y}{\partial \xi} & \frac{\partial y}{\partial \eta} \end{vmatrix} \tag{11}$$

Let G be the product matrix $H^T H$ where ^{T} denotes the transpose matrix with elements $g_{11}, g_{12}, g_{21}, g_{22}$. Let G^{-1} be the inverse of matrix G with elements $g^{11}, g^{12}, g^{21}, g^{22}$.

The U, V velocity components in the computational domain are given as:

$$\begin{bmatrix} U \\ V \end{bmatrix} = G^{-1} \begin{bmatrix} \frac{\partial \Phi}{\partial \xi} \\ \frac{\partial \Phi}{\partial \eta} \end{bmatrix} \tag{12}$$

while the u, v velocity components in the physical domain are:

$$\begin{bmatrix} u \\ v \end{bmatrix} = H \begin{bmatrix} U \\ V \end{bmatrix} \tag{13}$$

The continuity equation in the local system is:

$$\frac{\partial(\rho h U)}{\partial \xi} + \frac{\partial(\rho h V)}{\partial \eta} 0 \tag{14}$$

where h is the determinant of matrix H.

Numerical formulation

The physical interpretation of the quantities $\rho h U, \rho h V$ is that these are the mass fluxes across the faces $\xi =$ constant, $\eta =$ constant of the secondary cell, as shown in Fig 3. Derivatives of x at the primary or secondary finite-volume centres $\xi = 0, \eta = 0$ are calculated from:

$$\begin{aligned}
\left(\frac{\partial x}{\partial \xi}\right)_{i,j} &= \frac{x_{i,j+1} - x_{i,j-1}}{2} \\
\left(\frac{\partial x}{\partial \eta}\right)_{i,j} &= \frac{x_{i+1,j} - x_{i-1,j}}{2}
\end{aligned} \tag{15}$$

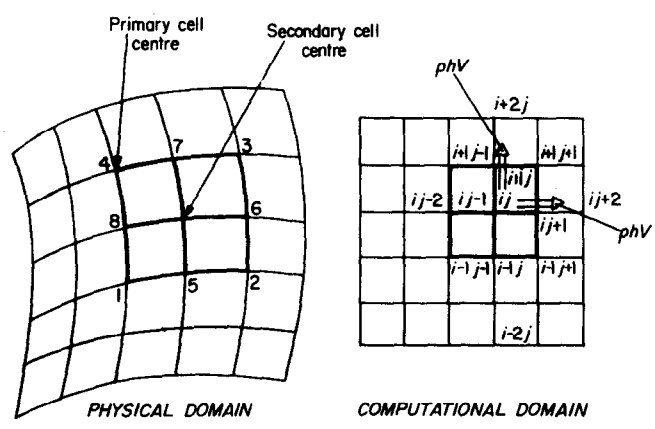

Fig 3 A secondary cell interlocks nine primary cells

Similar expressions hold for any of the quantities $y, \Phi, \rho hU, \rho hV$.

In a sense this discrete approximation is a direct finite-element method in which the finite-element representation of the solution in terms of nodal values and prescribed functions within the elements is directly substituted into the governing equations to obtain the nodal value equations. The formula for the local flux balance can be written down by applying it to the secondary cells centred at i, j. The discretisation is made possible by using partial derivatives introduced above. Thus:

$$(\rho hU)_{i,j+1}-(\rho hU)_{i,j-1}+(\rho hV)_{i+1,j}-(\rho hV)_{i-1,j}=0 \tag{16}$$

The approximation of the local velocity components is given by:

$$\begin{aligned} U_{i,j} &= g^{11}_{i,j}\left[\frac{\Phi_{i,j+1}-\Phi_{i,j-1}}{2}\right] + g^{12}_{i,j}\left[\frac{\Phi_{i+1,j}-\Phi_{i-1,j}}{2}\right] \\ V_{i,j} &= g^{21}_{i,j}\left[\frac{\Phi_{i,j+1}-\Phi_{i,j-1}}{2}\right] + g^{22}_{i,j}\left[\frac{\Phi_{i+1,j}-\Phi_{i-1,j}}{2}\right] \end{aligned} \tag{17}$$

Thus the discrete approximation of the governing flow equation in the local coordinate system is:

$$\begin{aligned} &a_1\Phi_{i-1,j-1}+a_2\Phi_{i-1,j+1}+a_3\Phi_{i+1,j+1}+a_4\Phi_{i+1,j-1} \\ &+a_5\Phi_{i-2,j}+a_6\Phi_{i,j+2}+a_7\Phi_{i+2,j}+a_8\Phi_{i,j-2}+a_9\Phi_{i,j}=0 \end{aligned} \tag{18}$$

where the $a_1, a_2, \ldots a_9$ are functions of the ρ, h, g^{ij} at appropriate nodal positions[8].

Transonic flow

The above analysis completes the definition of the discrete approximation scheme for main stream nodes in subsonic flow. Numerical formulation of the transonic problem, however, requires the construction of an appropriate set of differential equations. Problems encountered in the development of an efficient numerical algorithm for the calculation of transonic flows are:

- the equations governing the flow motion are highly non-linear;
- the flow is a mixed type with both subsonic and supersonic flows co-existing with the boundaries between them unknown; and
- the solution will in general contain shock waves, whose position is also unknown.

When the artificial compressibility method is applied (Appendix I), the continuity equation becomes:

$$\frac{\partial(\tilde{\rho}hU)}{\partial\xi}+\frac{\partial(\tilde{\rho}hV)}{\partial\eta}=0 \tag{19}$$

where:

$$\tilde{\rho}=\rho-\mu\frac{\partial\rho}{\partial s}\Delta s \qquad \frac{\partial\rho}{\partial s}\Delta s=\frac{U}{Q}\delta_\xi\rho\,\Delta\xi+\frac{V}{Q}\delta_\eta\rho\,\Delta\eta \tag{20}$$

with:

$$Q=(U^2+V^2)^{1/2} \qquad \mu=\max\left[0,\left(1-\frac{1}{M^2}\right)k\right] \tag{21}$$

k being typically 0.8 and upwind differencing is used in evaluating $\delta_\xi\rho\,\Delta\xi$, $\delta_\eta\rho\,\Delta\eta$ as follows

$$\begin{aligned} &\delta_\xi\rho\,\Delta\xi=\rho_{i,j}-\rho_{i,j-2} \quad \text{if } U_{i,j}>0 \\ &\delta_\xi\rho\,\Delta\xi=\rho_{i,j+2}-\rho_{i,j} \quad \text{if } U_{i,j}\leq 0 \\ &\delta_\eta\rho\,\Delta\eta=\rho_{i,j}-\rho_{i-2,j} \quad \text{if } V_{i,j}>0 \\ &\delta_\eta\rho\,\Delta\eta=\rho_{i+2,j}-\rho_{i,j} \quad \text{if } V_{i,j}\leq 0 \end{aligned} \tag{22}$$

This scheme maintains an upwind influence in the differentiation for supersonic points anywhere in the mesh for all possible orientations of the velocity vector. When the solution is converged, the application of the mass conservation and energy equation to the series of interlocking finite-volumes will yield zero net-flux into each element so that overall mass and energy are conserved. From the above it is evident that the transonic flow analysis applies when the shock waves are weak ($M \leq 1.3$), ie entropy does not increase across mass conservative shock jump regions.

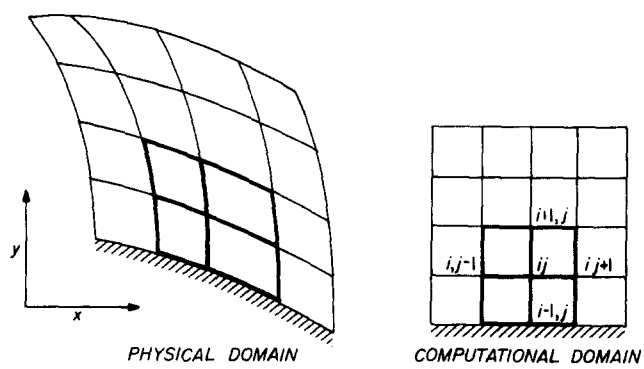

Fig 4 Boundary cell for the second computational row (i = 3, j = 1, JM)

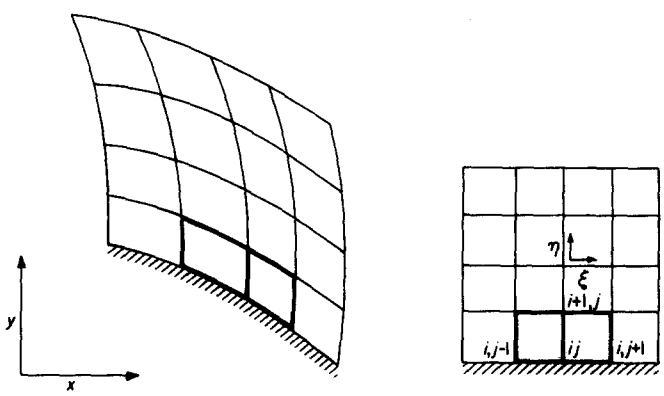

Fig 5 Boundary cell for first computational row (i = 2, j = 1, JM)

Boundary conditions

Suction and pressure surface

When the continuity equation in the local coordinate system is applied, the fluxes are taken across the faces of the secondary cell which is bounded on one face by the body surface. Fig 5 shows the boundary cell for the computational grid points lying on the first row. Half the cell is hidden inside the solid surface. When the flux balance is established on the secondary cell i, j the flux through the solid body of the blade must be zero, ie $\rho h V_{i,j} = 0$. The flux along the η direction at the $i+1, j$ grid point lying in the flowfield is taken over twice the area of the flux along the ξ direction.

Due to the complexity of the finite-volume it is evident that the next computational grid points lying on the second row will still have one face bounded by the blade solid surface, shown in Fig. 4. Similar analyses are applied for the upper 'pressure' blade surface.

Periodic boundaries and Kutta–Joukowski condition

It will be assumed that the flow is identical in each blade passage of the machine so that only one passage needs to be considered (Fig 6). The boundary conditions at the inlet lines AB $(A'B')$ are subject to the condition of periodicity specified by the equality of the complete velocity vector and the tangential velocity components at corresponding periodic points of the two lines. It follows that values of Φ at corresponding points can differ only by a constant amount $\Delta\Phi_{in}$, thus,

$$\Phi_{A'B'} = \Phi_{AB} + \Delta\Phi_{in} \tag{23}$$

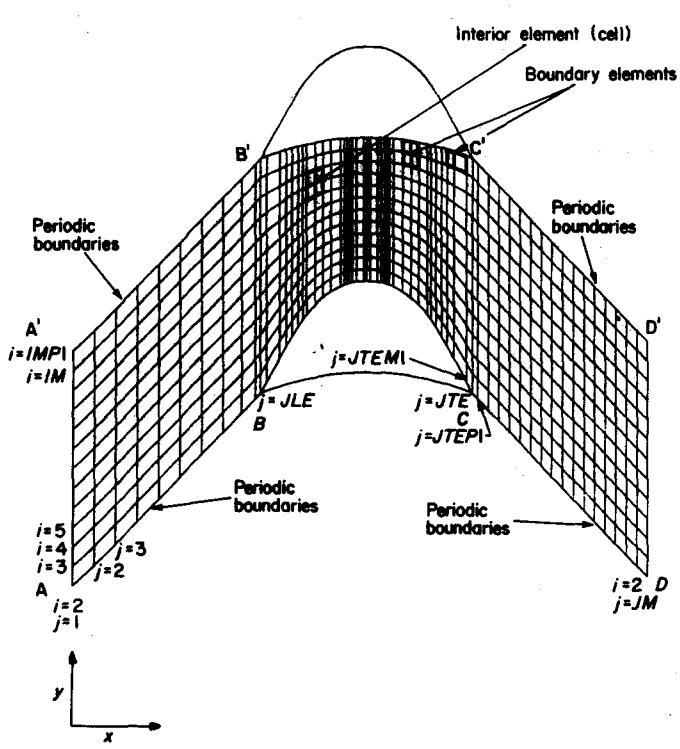

Fig 6 Cascade geometry and finite-volume elements (cells)

where $\Delta\Phi_{in}$ determines the mean pitchwise velocity at the inlet region of the cascade. On the lines $CD(C'D')$ formed by the extensions from the blade surfaces in the outlet region, the boundary conditions are also subject to a condition of periodicity specified by the equality of the magnitude of the velocity vector and of the tangential velocity components at corresponding periodic points. Thus:

$$\Phi_{C'D'} = \Phi_{CD} + \Delta\Phi_{out} \tag{24}$$

The $\Delta\Phi_{out}$ must be found through an iterative procedure so as to satisfy the Kutta condition on the blades. This condition demands equal pressures to be obtained at the control points of the elements adjacent to the trailing edges (Fig. 6). The $\Delta\Phi_{out}$ is calculated from:

$$\Delta\Phi_{out} = \Phi_{IMP1,JTEP1} - \Phi_{2,JTEP1} \tag{25}$$

where:

$$\Phi_{IMP1,JTEP1} = \Phi_{IMP1,JTEM1} + \frac{q_{2,JTE}}{q_{IMP1,JTE}}(\Phi_{IMP1,JTEP1} - \Phi_{IMP1,JTEM1}) \tag{26}$$

with $JTEP1 = JTE + 1$ and $JTEM1 = JTE - 1$ (JTE is the last computational grid point on the blade surface). When converged, then $q_{2,JTE} = q_{IMP1,JTE}$.

For non-lifting cases and for nozzle flow calculations, the current version of the numerical code skips the whole potential jump evaluation process.

Numerical resolution

A numerical algorithm has been presented for transonic flow calculations in turbomachinery blade rows. Iterations were continued until the average change of axial velocity between successive iterations dropped below 0.001%. Run time per point per iteration was 2.2×10^{-4} s on IBM 370-165 computer. Total number of iterations required for convergence was about 300 depending upon the geometry complexity and type of flow (subsonic-supersonic). Total CPU time for 7×50 grid points mesh was about 30 seconds on the above computer.

For subsonic flows, the central difference representations are accurate to second order, while in supersonic regions the difference approximation is a combination of the second order central difference (subsonic regions) with the first order accurate upwind approximation resulting from the artificial compressibility addition for supersonic regions. As the flow becomes increasingly supersonic, the scheme is increasingly retarded in the upwind direction. The choice of factor k in the equation:

$$\mu = \max\left[0, \left(1 - \frac{1}{M^2}\right)k\right] \tag{27}$$

strongly affects the accuracy of the solution but not the stability of the scheme. Errors associated with values of the factor k higher than 0.8 are increased Mach numbers in the subsonic regions of the blade suction surface while for supersonic regions, on the same blade surface, the Mach number is significantly decreased.

The most common source of inaccuracy arises at a blunt leading edge where the relatively coarse grid cannot resolve adequately the rapid changes in the flow properties. A large number of grid points must be used to obtain an accurate solution around a blunt leading edge.

Many other forms of discrete approximation of the partial differential equations could have been selected by altering the order of the finite elements involved. With the current code, sufficient flexibility exists for special regions of mesh where resolution is otherwise inadequate due to steep gradients in the dependent variable.

The numerical scheme can be used with any grid formation which need not be uniformly spaced in either coordinate direction. The grid is not restricted to that shown. Many mesh generation techniques can be adapted provided that grid periodicity is maintained.

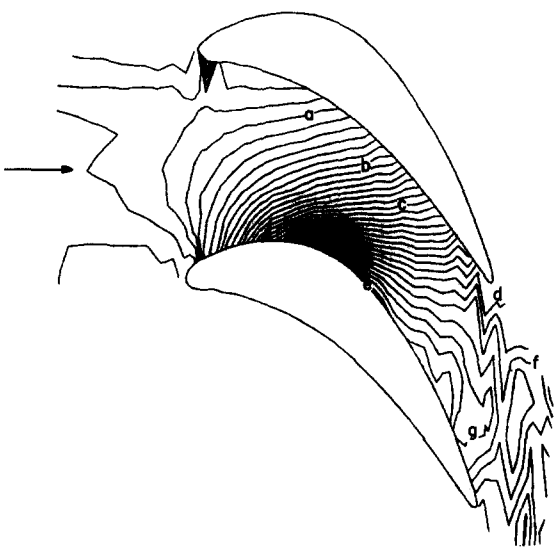

Fig 7 Calculated contours of equal Mach number (a–0.3340; b–0.4460; c–0.5850; d–0.7440; e–0.8569; f–0.7630; g–0.8180) for NASA nozzle turbine cascade at* $M_1^* = -0.231$

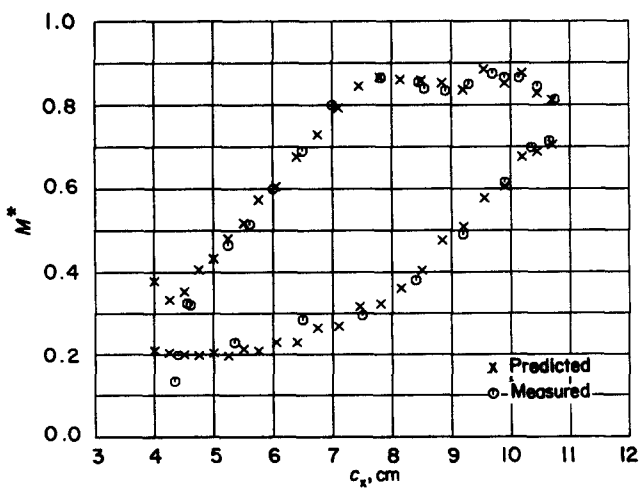

Fig 8 Comparison between measured and finite-volume predictions for blade surface Mach number distributions for NASA nozzle turbine cascade at* $M_1^* = 0.231$

Applications

Subsonic flow in a NASA turbine stator cascade

The first compressible flow test is an untwisted nozzle, tested by Whitney *et al*[9] in a parallel walled annulus. The problem selected is flow at the mean diameter section operating at the design mass flow rate with inlet $M_1^* = 0.231$ parallel to the axial direction. The experimental exit flow angle, which is also the total flow turning angle, was found to be −67.25°. Fig 7 shows the cascade geometry and the calculated contours of equal Mach* number in the flowfield. Comparison between theory and experiment is shown in Fig 8. Although the agreement is satisfactory, some differences appear on the blade pressure surface at about 30% of the blade chord downstream of the leading edge. Calculated flow angle was found to be −66.30°.

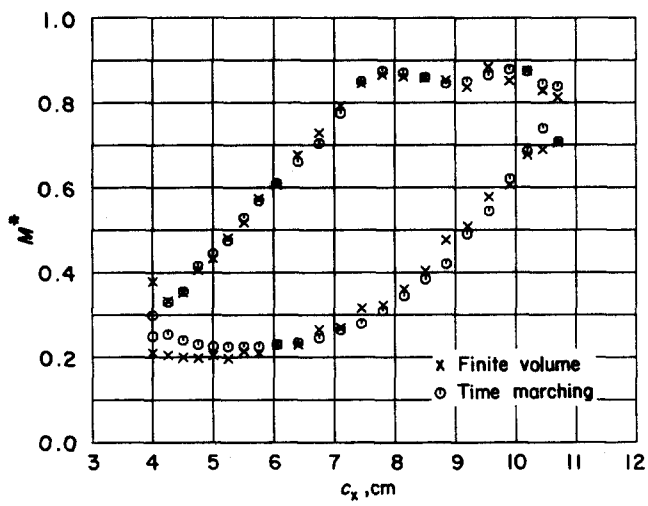

Fig. 9 Comparison between finite-volume and time-marching predictions for blade surface Mach number distributions for NASA nozzle turbine cascade at* $M_1^* = 0.231$

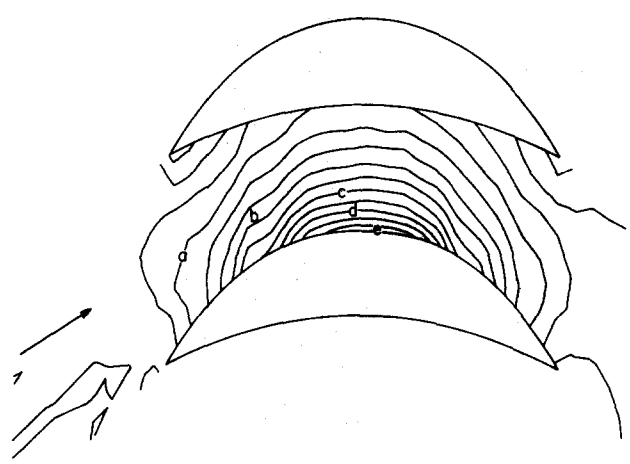

Fig 10 Calculated contours of equal Mach (a–0.664; b–0.816; c–0.923; d–1.008; e–1.097) number for Hobson's second impulse cascade at* $M_2^* = 0.61$

Comparison between the finite-volume and Denton's method[3] is shown in Fig 9; the agreement is good. In both methods an identical computational grid was used; this includes cusps at the leading and trailing edges of the blade to avoid discontinuities in geometry.

Transonic flow in Hobson's second impulse cascade

An impulse blade was designed and tested by Hobson[10] in the transonic wind tunnel at the Whittle Laboratory. Fig 10 shows the Hobson's second impulse cascade geometry and the calculated contours of equal M^*. The blade is symmetrical about the mid-chord. The critical Mach number at the cascade inlet, M_1^*, is 0.61 which is also the cascade outlet critical Mach number. The inlet flow direction is 46.10° and it is equal to the exit flow direction in absolute terms.

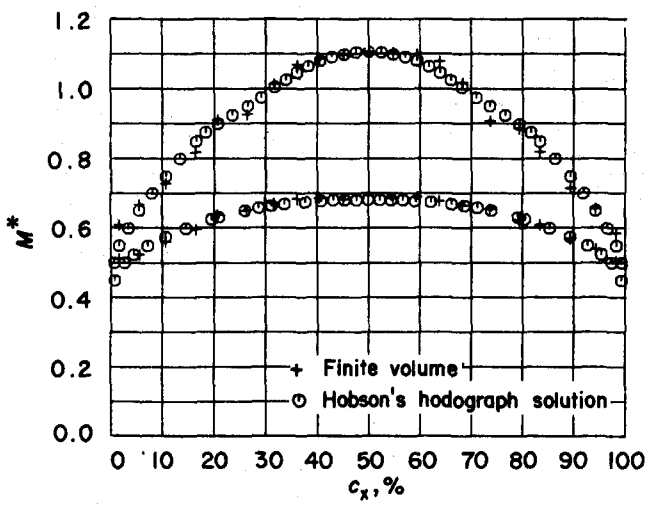

Fig 11 Comparison between Hobson's hodograph design and the finite-volume solution of the blade surface Mach number distribution for Hobson's second impulse cascade at* $M_2^* = 0.61$

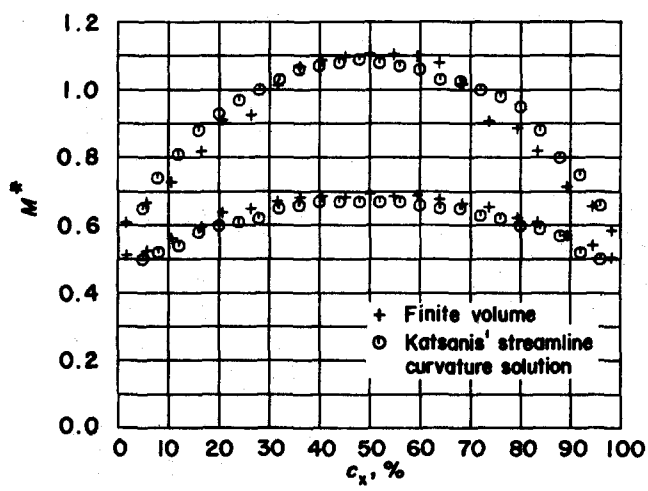

Fig 12 Comparison between Katsanis' streamline curvature solution and the finite-volume solution of the blade surface Mach number distribution for Hobson's second impulse cascade at* $M_2^* = 0.61$

Comparison between the calculated results and the analytical data, obtained from Hobson's hodograph design, is shown in Fig 11. The agreement is remarkably good. The Mach number distribution preserves the symmetry of the blade geometry. The calculated exit flow angle is −46.37°. Calculated results are also compared with those taken from a transonic streamline curvature method written by Katsanis[11]. Although the agreement between the two solutions is good, the maximum differences, $\delta M^* = 0.07$, occur on the first and last 30% of the blade suction surface (Fig 12).

Transonic flow in a turbine rotor of Rotor-Derby profile

The method has been used to determine the flow field within a transonic cascade of Rotor-Derby (RD) profile turbine rotor blades, shown in Fig 13 with the calculated contours of equal M. Experimental data has been provided from commissioning tests[12] carried out in the transonic wind tunnel at the Whittle Laboratory and from similar tests performed on the same blade profile at the DFVLR-AVA Gottingen, Germany.

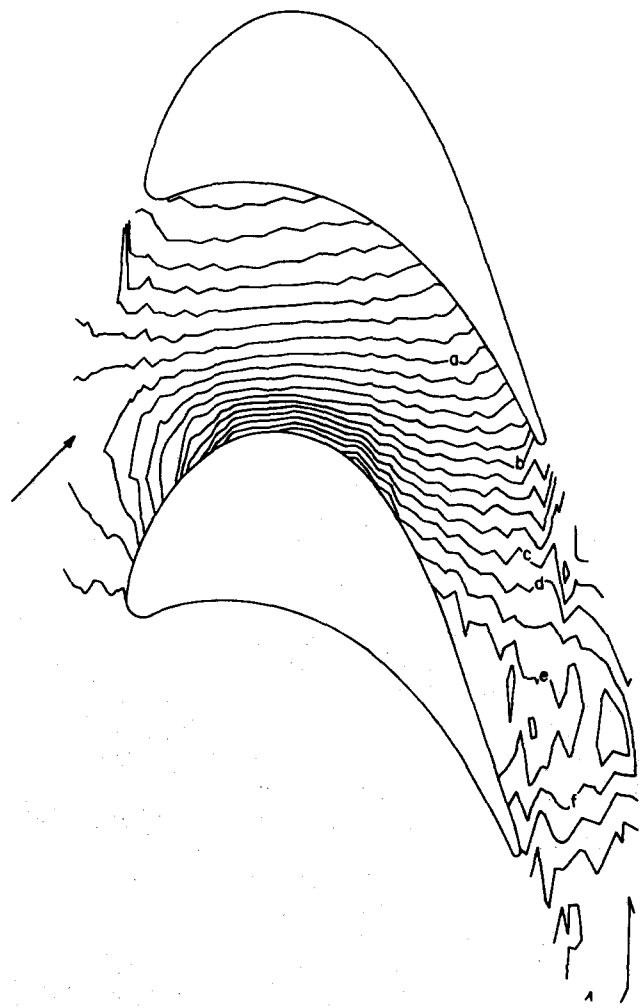

Fig 13 Calculated contours of equal Mach number (a–0.645; b–0.916; c–1.149; d–1.213; e–1.262; f–1.319) at $i = 0°$ ($\beta_1 = 56.0°$) *and* $M_2 = 1.194$ *for RD turbine rotor cascade*

Experimental local Mach number distributions on the blade surfaces, taken at DFVLR-AVA, with an inlet flow angle β_1 of 56.0° for a range of isentropic exit flow Mach numbers of $M_2 = 0.85$, 1.0, 1.12, and 1.181 are shown in Fig 14. Calculated local Mach number distributions at the same inlet flow angle for $M_{2is} = 0.916$, 0.996, 1.094, 1.194 are shown in Fig 15. All applied exit flow conditions have produced choked flow through the cascade.

Direct comparison of the calculated and measured (Whittle Laboratory) results at $M_{2is} = 0.916$ and $\beta_1 = 56.0°$ is shown in Fig 16. The overall Mach number distribution is in good agreement with the experiment. Calculated results give:

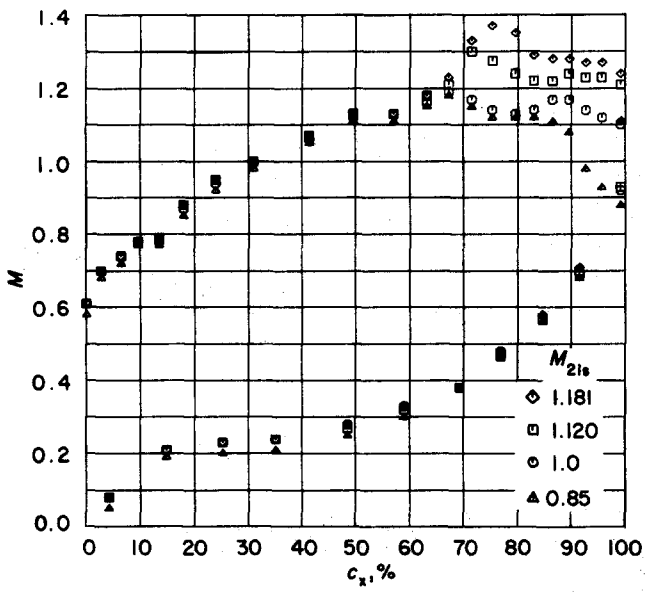

Fig 14 Experimental DFVLR-AVA, blade surface Mach number distribution at i = 0° ($\beta_1 = 56.0°$) *and* $M_{2is} = 0.85$, 1.0, 1.12, 1.181 *for RD turbine rotor cascade*

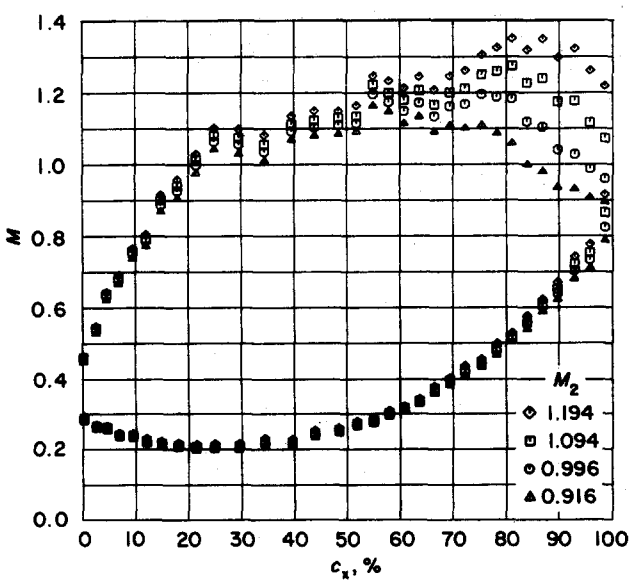

Fig 15 Predicted blade surface Mach number distribution at i = 0° ($\beta_1 = 56.0°$) *and* $M_2 = 0.916$, 0.996, 1.094, 1.194 *for RD turbine rotor cascade*

$\beta_1 = 56.0°$ $M_1 = 0.460$

$\beta_2 = -66.7°$ $M_2 = 0.916$

measured results give:

$\beta_1 = 56.0°$ $M_1 = 0.449$

$\beta_2 = -66.8°$ $M_2 = 0.914$

Comparison between theory and experiment (DFVLR-AVA) at the highest exit flow condition, $M_{2is} = 1.194$, is shown in Fig 17. The comparison worsens at about 20–30% of blade axial chord length on the suction surface where there is high flow turning. Measured results show a shock-wave at 75% of the blade axial chord while Schlieren pictures taken at the Whittle Laboratory show a shock-boundary layer interaction which leads to local separation of the boundary layer with slow re-attachment.

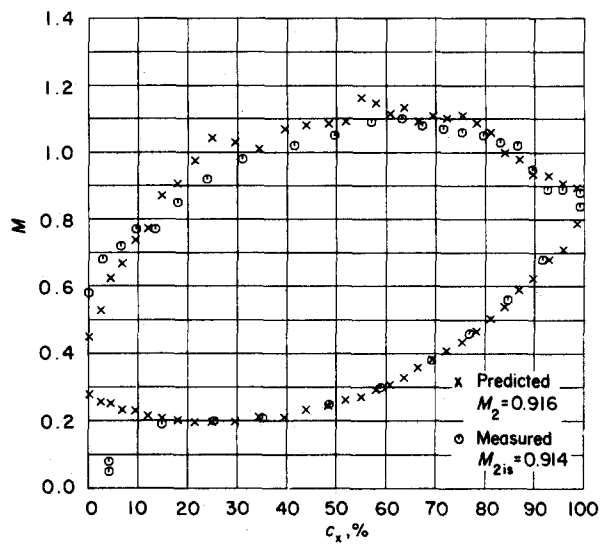

Fig 16 Comparison between measured (Whittle Laboratory) and predicted blade surface Mach number distribution at i = 0° ($\beta_1 = 56.0°$) *and* $M_2 = 0.916$ *for RD turbine rotor cascade*

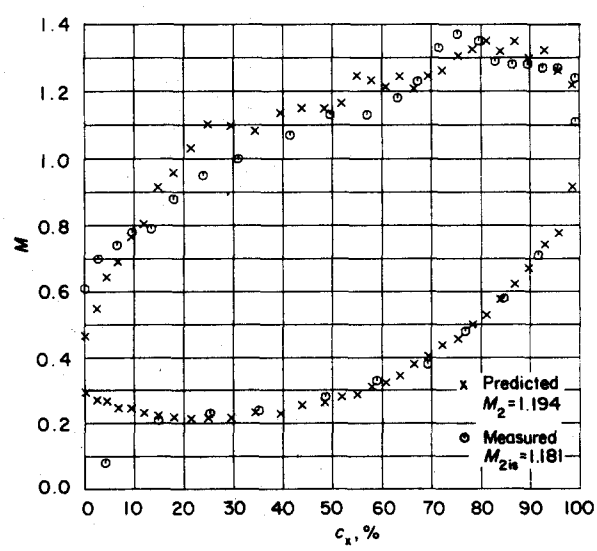

Fig 17 Comparison between measured (DFVLR-AVA) and predicted blade surface Mach number distribution at i = 0° ($\beta_1 = 56.0°$) *and* $M_2 = 1.194$ *for RD turbine rotor cascade*

Conclusions

A finite-difference scheme resulting from a second order finite element shape function has been applied to arbitrary turbomachinery geometries using a body fitted non-orthogonal local coordinate system. It is able to calculate 2-D potential flows in the incompressible, subsonic, transonic and shock-free supersonic flow speed range. The main advantage of the method is the ease of treatment of exact blade surface boundary conditions. This has been achieved by transformation of the usually highly curved turbomachinery blade surfaces to coordinate lines of the computational domain. Stability in supersonic regions is maintained by the addition of an artificial compressibility term. This greatly simplifies the numerical procedure and effectively allows a mixed elliptic hyperbolic problem to be solved by an elliptic solution procedure. The method has been applied to a variety of turbomachinery blade profiles in order to validate its potentialities.

Numerical results indicate that the finite-volume code is an accurate, reliable and fast method for predicting the irrotational inviscid, transonic, 2-D flow through all types of turbomachinery blades.

References

1 **Hafez M. M., Murmann E. M. and South J. C.** Artificial compressibility methods for numerical solution of transonic full potential equation. *AIAA Paper No 78-1148 July 1978*

2 **Gopalakrishnan S. and Bozzola R. A.** Numerical technique for the calculation of transonic flow in turbomachinery cascades. *ASME Paper No 71-GT-42, 1971*

3 **Denton J. D.** A time marching method for two and three dimensional blade to blade flows. *Aeronautical Research Council R&M, 3775, 1975*

4 **Caspar J. R., Hobbs D. E., and Davies, R. L.** The calculation of two dimensional compressible potential flow in cascades using finite area techniques. *AIAA 17th Aerospace New Orleans 1979*

5 **Acay H. V. and Ecer A.** Transonic flow computations in cascades using a finite-element method. *ASME Paper No. 81-GT-4 1981*

6 **Habashi W. G., Dueck E. G. and Kenny D. P.** Finite-element approach to compressor blade to blade cascade analysis. *AIAA Journal, July 1979* **17**(7)

7 **Farrell C. and Adamczyck J.** Full potential solution of transonic quasi-3-D flow through a cascade using artificial compressibility. *ASME, No. 81-GT-70 1981*

8 **Soulis J. V.** Calculation of transonic potential flow through turbomachinery blade rows. *Ph.D. Thesis Cambridge University 1982*

9 **Whitney, W. J. et al** Cold air investigation of a turbine for high temperature engine application. I-turbine design and overall engine performance. *NASA TN D-3751, 1967*

10 **Hobson D. E.** Shock-free transonic flow in turbomachinery cascades. *Ph.D. Thesis, Cambridge University 1974*

11 **Katsanis T.** Fortran program for calculating transonic velocities on a blade to blade surface of a turbomachine. *NASA Report No TND-5427 1970*

12 **Camus J-J.** Transonic cascade tunnel commissioning tests 2 RD profile. *Cambridge University Engineering Department CUED/A-Turbo/TR-103 1979*

Appendix I

For 2-D full potential equations the corresponding 'viscous' transonic flow equation can be written[1]:

$$-\frac{\rho}{a^2}[(a^2-q^2)\Phi_{ss}+a^2\Phi_{nn}]=\frac{\rho}{a^2}\Delta s(a^2-q^2)\Phi_{sss} \quad (I.1)$$

where s and n are coordinates in the local stream and normal directions, and the right-hand side equals:

$$\frac{\rho}{a^2}\Delta s(a^2-q^2)\left[\frac{u}{q}\left(\frac{u^2u_x+2uvv_x+v^2v_y}{q^2}\right)_x + \frac{v}{q}\left(\frac{u^2u_x+2uvu_y+v^2v_y}{q^2}\right)_y\right] \quad (I.2)$$

because:

$$\Phi_{sss}=\frac{u}{q}(\Phi_{ss})_x+\frac{v}{q}(\Phi_{ss})_y \quad (I.3)$$

and:

$$\Phi_{ss}=\frac{u^2}{q^2}\Phi_{xx}+\frac{2uv}{q^2}\Phi_{xy}+\frac{v^2}{q^2}\Phi_{yy} \quad (I.4)$$

The first bracket term of Eq (I.2) is written as:

$$-\frac{\rho}{a^2}\Delta s\left(1-\frac{a^2}{q^2}\right)q^2\left[\frac{u}{q}\left(\frac{u^2u_x+2uvv_x+v^2v_y}{q^2}\right)_x\right] \quad (I.5)$$

an equivalent expression is given by:

$$\left[\left(1-\frac{a^2}{q^2}\right)u\,\Delta s\left[\frac{u}{q}\left(-\frac{\rho}{a^2}\right)(uu_x+vv_x) + \frac{v}{q}\left(-\frac{\rho}{a^2}\right)(uu_y+vv_y)\right]\right]_x \quad (I.6)$$

or:

$$\left[\mu u\Delta s\left(\frac{u}{q}\rho_x+\frac{v}{q}\rho_y\right)\right]_x \quad (I.7)$$

with:

$$\mu=\left(1-\frac{a^2}{q^2}\right) \quad (I.8)$$

because:

$$\rho_x=-\frac{\rho}{a^2}(uu_x+vv_x) \quad \text{and} \quad \rho_y=-\frac{\rho}{a^2}(uu_y+vv_y) \quad (I.9)$$

thus:

$$(\mu u\rho_s\,\Delta s)_x \quad (I.10)$$

Similarly the second member of the bracket yields:

$$(\mu v\rho_s\,\Delta s)_y \quad (I.11)$$

Thus the continuity equation (I.1) is written:

$$(\rho u)_x+(\rho v)_y=(\mu u\rho_s\,\Delta s)_x+(\mu v\rho_s\Delta s)_y \quad (I.12)$$

or:

$$(\tilde{\rho}u)_x+(\tilde{\rho}v)_y=0 \quad (I.13)$$

with

$$\tilde{\rho}=\rho-\mu\rho_s\,\Delta s \quad (I.14)$$